

# Position-Aware Scene-Appearance Disentanglement for Bidirectional Photoacoustic Microscopy Registration

Yiwen Wang and Jiahao Qin<sup>\*</sup>

**Abstract.** High-speed optical-resolution photoacoustic microscopy (OR-PAM) with bidirectional raster scanning doubles imaging speed but introduces coupled domain shift and geometric misalignment between forward and backward scan lines. Existing registration methods, constrained by brightness constancy assumptions, achieve limited alignment quality, while recent generative approaches address domain shift through complex architectures that lack temporal awareness across frames. We propose GPEReg-Net, a scene-appearance disentanglement framework that separates domain-invariant scene features from domain-specific appearance codes via Adaptive Instance Normalization (AdaIN), enabling direct image-to-image registration without explicit deformation field estimation. To exploit temporal structure in sequential acquisitions, we introduce a Global Position Encoding (GPE) module that combines learnable position embeddings with sinusoidal encoding and cross-frame attention, allowing the network to leverage context from neighboring frames for improved temporal coherence. On the OR-PAM-Reg-4K benchmark (432 test samples), GPEReg-Net achieves NCC of 0.953, SSIM of 0.932, and PSNR of 34.49 dB, surpassing the state-of-the-art by 3.8% in SSIM and 1.99 dB in PSNR while maintaining competitive NCC. Code is available at <https://github.com/JiahaoQin/GPEReg-Net>.

**Keywords:** Photoacoustic microscopy · Image registration · Scene-appearance disentanglement · Position encoding

## 1 Introduction

Optical-resolution photoacoustic microscopy (OR-PAM) combines the cellular-level spatial resolution of optical imaging with the sensitivity of photoacoustic detection, enabling label-free visualization of endogenous chromophores such as hemoglobin, melanin, and lipids [22, 26, 27]. High-speed OR-PAM systems employ bidirectional raster scanning [25, 6] to nearly double the imaging frame rate, facilitating the capture of rapid hemodynamic events in *in vivo* cerebral microvasculature [24, 5].

However, bidirectional scanning introduces systematic artifacts that severely compromise image quality. Forward and backward scan lines exhibit coupled domain shift and geometric misalignment arising from mechanical hysteresis, velocity asymmetry, and scan-direction-dependent system response [19, 10]. These

---

<sup>\*</sup> Corresponding author: jiahao.qin19@gmail.com

artifacts manifest as spatial offsets between adjacent columns and intensity differences that violate the brightness constancy assumption underlying conventional registration methods [4].

Existing approaches to this problem fall into two categories. Classical registration methods, including SIFT [9], Demons [21], optical flow [7], and SyN [1], attempt direct spatial alignment but achieve limited accuracy ( $\text{NCC} \leq 0.72$ ) because they cannot compensate for intensity differences between forward and backward acquisitions. Recent deep learning methods such as VoxelMorph [2] and TransMorph [3] learn to predict deformation fields but similarly assume comparable intensity distributions, yielding suboptimal results under domain shift. Domain-invariant registration [16] and scene-appearance separation frameworks [12] address domain shift through disentangled representations, achieving NCC of 0.96, and progressive contrast-guided approaches [11] further improve alignment through coarse-to-fine refinement, but these methods employ complex architectures and lack awareness of temporal context across frames.

We observe two key opportunities. First, the domain shift in bidirectional OR-PAM can be modeled as a style transfer problem: the underlying anatomical scene is shared between forward and backward scans, while the appearance (intensity profile) differs systematically. Adaptive Instance Normalization (AdaIN) [8] provides an elegant mechanism to inject target appearance into domain-invariant scene representations without requiring explicit deformation fields, analogous to how multimodal alignment methods [17] bridge heterogeneous feature spaces through learned transformations. Cross-modal representation learning [13] has further demonstrated the effectiveness of joint representation spaces for bridging domain gaps. Second, consecutive frames in OR-PAM acquisitions share substantial structural similarity, and exploiting this temporal context—via position-aware encoding inspired by transformer architectures [20]—can improve registration consistency across frames.

In this paper, we propose GPEReg-Net, a position-aware scene-appearance disentanglement framework for bidirectional OR-PAM registration. The core idea is to decompose each image into a domain-invariant scene representation and a global appearance code, then reconstruct the registered output by combining the scene features of the moving image with the appearance code of the fixed image through AdaIN modulation. A Global Position Encoding (GPE) module enriches scene features with temporal context from neighboring frames via learnable position embeddings and cross-frame attention. The main contributions are:

1. We propose a scene-appearance disentanglement framework with AdaIN-based modulation that enables cross-domain registration without explicit deformation field estimation, achieving SSIM of 0.932 and PSNR of 34.49 dB on OR-PAM-Reg-4K.
2. We introduce a Global Position Encoding (GPE) module combining learnable and sinusoidal position embeddings with multi-head cross-frame attention, providing temporal awareness for sequential OR-PAM acquisitions.

3. We conduct comprehensive evaluation on two OR-PAM benchmarks, demonstrating that the scene-appearance disentanglement approach surpasses the state-of-the-art in SSIM and PSNR on OR-PAM-Reg-4K, while analysis on OR-PAM-Reg-Temporal-26K reveals limitations of fixed-frame position embeddings under high temporal variability.

## 2 Method

### 2.1 Overview

The proposed framework takes as input a pair of column images: the moving image  $I_m$  (even/backward scan columns) and the fixed image  $I_f$  (odd/forward scan columns), both of size  $H \times W$ . The goal is to produce a registered output  $\hat{I}_r$  that is aligned with  $I_f$  in both geometry and intensity.

As illustrated in fig. 1, the framework consists of four modules:

1. **SceneEncoder  $\mathcal{S}$** : Extracts domain-invariant scene features  $\mathbf{s} = \mathcal{S}(I_m)$  via instance normalization, discarding appearance information.
2. **AppearanceEncoder  $\mathcal{A}$** : Extracts a global appearance code  $\mathbf{a} = \mathcal{A}(I_f)$  that captures the intensity profile of the target domain.
3. **Global Position Encoding  $\mathcal{G}$** : Enhances scene features with temporal context:  $\tilde{\mathbf{s}} = \mathcal{G}(\mathbf{s}, t)$ , where  $t$  is the frame index.
4. **ImageDecoder  $\mathcal{D}$** : Reconstructs the registered output using AdaIN modulation:  $\hat{I}_r = \mathcal{D}(\tilde{\mathbf{s}}, \mathbf{a})$ .

### 2.2 Scene Encoder

The SceneEncoder follows a U-Net-style [18] architecture to extract domain-invariant features from the moving image. To achieve domain invariance, we use Instance Normalization (IN) instead of Batch Normalization throughout the encoder, as IN normalizes each sample independently, removing per-instance style information while preserving spatial structure.

The encoder processes the single-channel input through four resolution levels with channel dimensions  $C_l \in \{32, 64, 128, 256\}$ . Each level consists of two convolutional blocks ( $\text{Conv}_{3 \times 3}$ -IN-LeakyReLU) followed by  $2 \times$  max pooling for downsampling. The decoder mirrors the encoder, using bilinear upsampling and skip connections that concatenate encoder features at matching resolutions. A final  $1 \times 1$  convolution projects the 32-channel output to a 64-dimensional scene feature map  $\mathbf{s} \in \mathbb{R}^{64 \times H \times W}$ , which captures the structural content of the moving image while being invariant to domain-specific intensity patterns.

### 2.3 Appearance Encoder

The AppearanceEncoder extracts a compact global appearance vector from the fixed image that characterizes its intensity distribution. The architecture consists

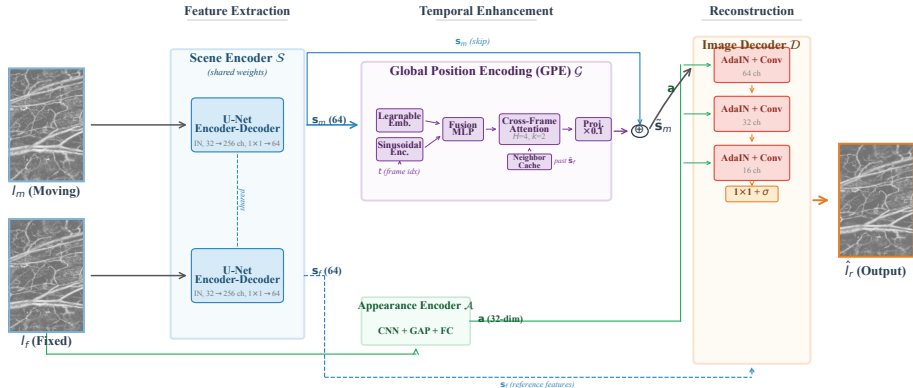


**Fig. 1.** Overview of the GPEReg-Net framework. The SceneEncoder extracts domain-invariant features  $s$  from the moving image using instance normalization and skip connections. The AppearanceEncoder extracts a 32-dim global appearance code  $a$  from the fixed image. The GPE module enriches scene features with temporal context from neighboring frames via learnable position embeddings, sinusoidal encoding, and cross-frame attention. The ImageDecoder uses AdaIN to modulate scene features with the target appearance at each decoding level, producing the registered output  $\hat{l}_r$ .

of four stride-2 convolutional layers ( $1 \rightarrow 16 \rightarrow 32 \rightarrow 64 \rightarrow 128$  channels, each followed by LeakyReLU) that progressively downsample the spatial dimensions. Global Average Pooling (GAP) collapses the spatial dimensions, producing a 128-dimensional vector that is passed through two fully connected layers ( $128 \rightarrow 64 \rightarrow 32$ ) with ReLU activation, yielding the appearance code  $a \in \mathbb{R}^{32}$ .

The appearance code  $a$  is a low-dimensional summary of the target domain's global intensity characteristics. By design, it discards spatial information (via GAP) and retains only domain-specific statistics, complementing the scene features that encode spatial structure but discard appearance.

## 2.4 Image Decoder with AdaIN Modulation

The ImageDecoder reconstructs the registered output by injecting the target appearance into the domain-invariant scene features using Adaptive Instance Normalization (AdaIN) [8]. Given scene features  $s$  and appearance code  $a$ , the AdaIN operation at each decoder block is:

$$\text{AdaIN}(s, a) = \gamma(a) \cdot \frac{s - \mu(s)}{\sigma(s)} + \beta(a), \quad (1)$$

where  $\mu(s)$  and  $\sigma(s)$  are the channel-wise mean and standard deviation of the scene features, and  $\gamma(a)$ ,  $\beta(a)$  are affine parameters predicted from the appearance code via learned linear projections.

The decoder consists of three AdaIN blocks. Each block receives the scene features, applies AdaIN modulation with the appearance code, followed by  $\text{Conv}_{3 \times 3}$ -ReLU layers with bilinear upsampling. The three blocks operate at 64, 32, and 16 channels respectively, progressively reconstructing spatial resolution. A final  $1 \times 1$  convolution with sigmoid activation maps the 16-channel features to the single-channel registered output  $\hat{I}_r$ .

This design enables the network to transfer the intensity characteristics of the fixed image (odd/forward columns) onto the structural content of the moving image (even/backward columns) without estimating any spatial deformation field.

## 2.5 Global Position Encoding

The GPE module exploits temporal structure across sequential frames to improve registration consistency. It operates on the spatially averaged scene features and outputs a position-aware enhancement that is added to the scene features before decoding. The module consists of five components:

*Learnable position embedding.* A learnable embedding table  $\mathbf{E} \in \mathbb{R}^{N \times 64}$  stores a unique 64-dimensional vector for each of the  $N$  possible frame positions. Given frame index  $t$ , the embedding  $\mathbf{e}_t = \mathbf{E}[t]$  encodes the absolute temporal position.

*Sinusoidal position encoding.* Following the transformer positional encoding [20], a fixed sinusoidal encoding  $\mathbf{p}_t \in \mathbb{R}^{64}$  provides continuous frequency-based representation of frame index  $t$ :

$$\mathbf{p}_{t,2i} = \sin\left(\frac{t}{10000^{2i/64}}\right), \quad \mathbf{p}_{t,2i+1} = \cos\left(\frac{t}{10000^{2i/64}}\right), \quad (2)$$

where  $i$  indexes the embedding dimension. The sinusoidal encoding provides smooth interpolation between positions, complementing the learnable embedding's capacity to capture data-specific temporal patterns.

*Fusion MLP.* The learnable and sinusoidal encodings are concatenated and fused through a two-layer MLP ( $128 \rightarrow 64 \rightarrow 64$ , with ReLU activation):

$$\mathbf{g}_t = \text{MLP}([\mathbf{e}_t; \mathbf{p}_t]), \quad (3)$$

yielding the fused position encoding  $\mathbf{g}_t \in \mathbb{R}^{64}$  that combines the strengths of both representations.

*Cross-frame attention.* To incorporate temporal context from neighboring frames, a multi-head attention mechanism ( $H=4$  heads) attends to the features of  $k=2$  neighboring frames (stored in a running cache during sequential inference). The query is derived from the current frame's scene features (spatially averaged), while keys and values come from the neighbor cache:

$$\mathbf{c}_t = \text{MultiHead}(W_Q \bar{\mathbf{s}}_t, W_K \bar{\mathbf{S}}_{\mathcal{N}(t)}, W_V \bar{\mathbf{S}}_{\mathcal{N}(t)}), \quad (4)$$

where  $\bar{\mathbf{s}}_t$  is the spatially averaged scene feature of frame  $t$ ,  $\bar{\mathbf{S}}_{\mathcal{N}(t)}$  collects features from the  $k$  nearest neighbors, and  $W_Q, W_K, W_V$  are learned projection matrices.

*Position-to-scene projection.* The fused position encoding  $\mathbf{g}_t$  and cross-frame context  $\mathbf{c}_t$  are combined via element-wise addition and projected to the scene feature space through a linear layer. The result is added to the scene features with a scaling factor  $\alpha = 0.1$  to avoid disrupting the pre-trained scene representations:

$$\tilde{\mathbf{s}} = \mathbf{s} + \alpha \cdot W_{\text{proj}}(\mathbf{g}_t + \mathbf{c}_t), \quad (5)$$

where the projection is broadcast across spatial dimensions.

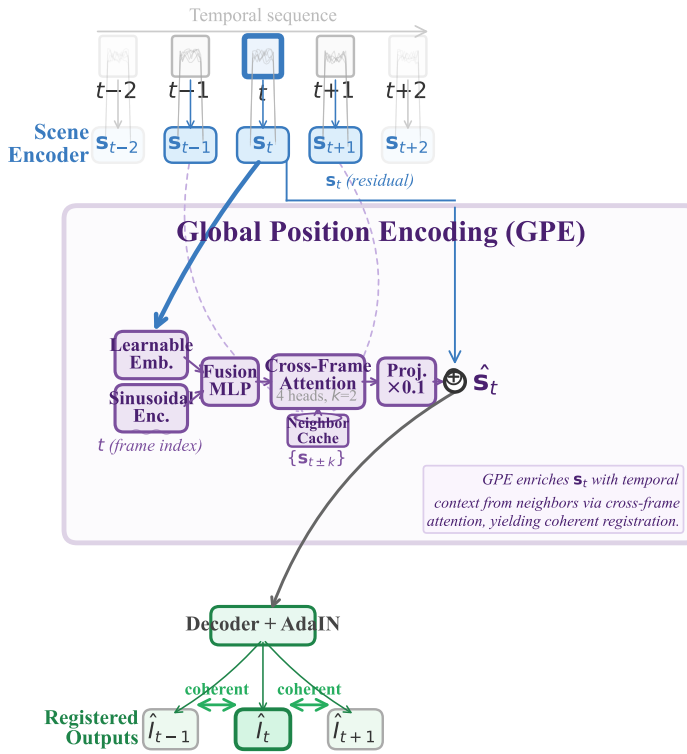


**Fig. 2.** Illustration of the GPE temporal mechanism. For each frame  $t$  in the temporal sequence, the Scene Encoder extracts domain-invariant features  $\mathbf{s}_t$ . The GPE module enriches  $\mathbf{s}_t$  with temporal context from neighboring frames via learnable and sinusoidal position encodings fused through an MLP, followed by multi-head cross-frame attention ( $H = 4$ ,  $k = 2$ ) over a running neighbor cache. The position-aware features  $\tilde{\mathbf{s}}_t$  are then decoded with AdaIN modulation to produce temporally coherent registered outputs.

## 2.6 Loss Function

The training objective combines pixel-wise reconstruction loss with a scene alignment regularizer:

$$\mathcal{L} = \mathcal{L}_{\text{recon}} + \lambda \cdot \mathcal{L}_{\text{scene}}, \quad (6)$$

where  $\mathcal{L}_{\text{recon}} = \|\hat{I}_r - I_f\|_1$  is the L1 reconstruction loss that encourages pixel-wise fidelity between the registered output and the fixed image, and  $\mathcal{L}_{\text{scene}} = \|\mathcal{S}(I_m) - \mathcal{S}(I_f)\|_2^2$  is an MSE loss on the scene features that encourages the SceneEncoder to produce consistent representations for corresponding image pairs regardless of domain. The weighting factor  $\lambda = 10.0$  reflects the importance of scene alignment for the disentanglement quality. This joint optimization of reconstruction and scene alignment objectives is inspired by multi-task learning principles [14], where shared representations benefit from complementary supervision. Notably, the scene alignment loss operates in the feature space rather than image space, providing a complementary training signal that reinforces domain invariance.

## 3 Experiments

### 3.1 Datasets and Implementation Details

*Datasets.* We evaluate on two benchmarks: (1) **OR-PAM-Reg-4K** [28], comprising 4,248 image pairs at  $512 \times 256$  resolution from three mice, split into training (3,396), validation (420), and test (432) sets; and (2) **OR-PAM-Reg-Temporal-26K** [29], containing 26,000+ temporally ordered pairs from longitudinal acquisitions, providing a more challenging evaluation with temporal drift and biological variability.

*Implementation.* GPEReg-Net contains 3.40M parameters. Training uses the Adam optimizer ( $\text{lr} = 10^{-4}$ , weight decay  $10^{-5}$ ) with cosine annealing over 30 epochs, batch size 8, and gradient clipping (max norm 1.0). Mixed precision (AMP) is employed for memory efficiency. All experiments use a single NVIDIA V100 GPU with seed 42 for reproducibility.

*Evaluation metrics.* Since ground-truth registered images are unavailable for bidirectional OR-PAM data, we adopt a reference-free evaluation strategy. For each frame  $i$ , the forward (odd) columns  $O_i$  serve as the pseudo ground truth for the registered backward (even) columns  $\hat{E}_i$ , and we report NCC, SSIM [23], and PSNR between  $O_i$  and  $\hat{E}_i$  to quantify intra-frame alignment quality.

For the temporally ordered 26K dataset, we additionally propose temporal consistency metrics to evaluate cross-frame coherence. Given consecutive merged frames  $M_i$  and  $M_{i+1}$  (formed by interleaving odd and registered even columns to reconstruct the full  $512 \times 512$  image), we define:

- **TNCC / TSSIM / TPSNR** (Temporal NCC / SSIM / PSNR): The mean NCC, SSIM, and PSNR computed between all consecutive merged frame pairs ( $M_i, M_{i+1}$ ). Higher values indicate better temporal coherence of the registered sequence.
- **TNCG / TSSG** (Temporal NCC Gap / SSIM Gap): Defined as  $TNCG = |\text{TNCC} - \text{TNCC}_{\text{ref}}|$  and  $TSSG = |\text{TSSIM} - \text{TSSIM}_{\text{ref}}|$ , where the reference values are computed from odd-only columns (the physical ceiling). Smaller gaps indicate that the registration preserves the natural inter-frame dynamics without introducing artificial temporal fluctuations.

### 3.2 Comparison with State-of-the-Art

table 1 presents the quantitative comparison on both benchmarks. The proposed method is compared against four traditional methods (SIFT, Demons, Optical Flow, SyN) and three deep learning methods (VoxelMorph, TransMorph, SAS-Net [12]).

**Table 1.** Intra-frame registration quality on OR-PAM-Reg-4K (432 test samples) and OR-PAM-Reg-Temporal-26K (2,714 test samples). NCC, SSIM, and PSNR measure alignment between odd and registered even columns. Best in **bold**, second best underlined.

Method	OR-PAM-Reg-4K			OR-PAM-Reg-Temporal-26K		
	NCC↑	SSIM↑	PSNR↑	NCC↑	SSIM↑	PSNR↑
<i>Traditional Methods</i>						
Unregistered	0.167	0.482	19.46	0.190	0.536	18.90
SIFT [9]	0.723	0.679	24.14	0.752	<u>0.745</u>	24.34
Demons [21]	0.323	0.579	20.35	0.347	0.634	20.12
Optical Flow [7]	0.061	0.455	18.99	0.089	0.516	18.80
SyN [1]	0.411	0.613	21.55	0.505	0.691	21.73
<i>Deep Learning Methods</i>						
VoxelMorph [2]	0.724	0.659	22.88	0.741	0.594	22.84
TransMorph [3]	0.594	0.641	21.09	0.693	0.653	22.07
SAS-Net [12]	<b>0.961</b>	<u>0.894</u>	<u>32.50</u>	<b>0.994</b>	<b>0.972</b>	<b>40.22</b>
<b>GPEReg-Net (Ours)</b>	<u>0.953</u>	<b>0.932</b>	<b>34.49</b>	<u>0.921</u>	0.634	27.22

*Performance on OR-PAM-Reg-4K.* Traditional registration methods achieve NCC below 0.73 on 4K due to the violation of brightness constancy by scan-direction-dependent domain shift. Among deep learning methods, deformation-based approaches (VoxelMorph, TransMorph) perform comparably to or below SIFT despite learning spatial transformations, confirming that the domain shift fundamentally limits correspondence estimation in pixel space. SAS-Net, which

explicitly addresses domain shift through scene-appearance separation, achieves the highest NCC of 0.961.

GPEReg-Net achieves NCC of 0.953 (competitive with SAS-Net), SSIM of 0.932 (+3.8% over SAS-Net’s 0.894), and PSNR of 34.49 dB (+1.99 dB over SAS-Net’s 32.50 dB). The SSIM and PSNR gains indicate that the AdaIN-based reconstruction produces sharper, more structurally faithful outputs compared to SAS-Net’s generative approach. By directly modulating scene features with appearance codes rather than estimating deformation fields, GPEReg-Net avoids the interpolation artifacts that degrade high-frequency structural details.

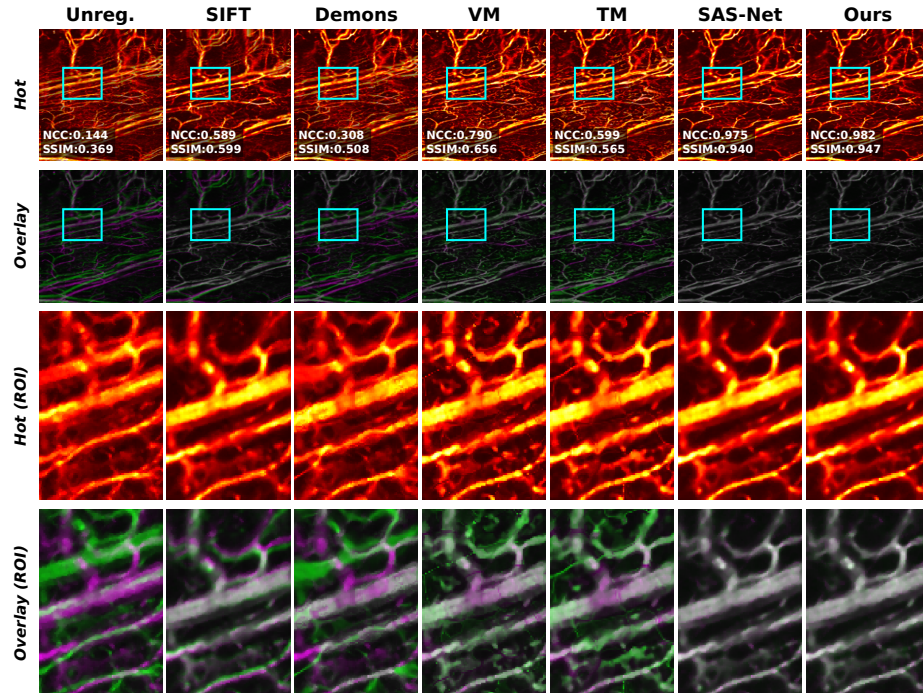


**Fig. 3.** Qualitative comparison of registration results on OR-PAM-Reg-4K. Each column shows one test sample. From top to bottom: fixed image (odd columns), moving image (even columns), and registered outputs from each method. GPEReg-Net produces visually sharper results with better structural preservation compared to deformation-based methods, and comparable quality to SAS-Net.

*Performance on OR-PAM-Reg-Temporal-26K.* On 26K, GPEReg-Net’s intra-frame quality degrades (NCC=0.921, SSIM=0.634, PSNR=27.22 dB), ranking below SAS-Net (NCC=0.994, SSIM=0.972, PSNR=40.22 dB). This performance gap reveals a key limitation: the GPE module’s learnable position embedding table is of fixed size, and the 26K dataset spans a much wider temporal range

with greater biological variability than the 4K dataset. The fixed-capacity embedding cannot adequately represent the diverse temporal patterns encountered in extended longitudinal sequences. Furthermore, the scene-appearance disentanglement, while effective for the moderate domain shift in 4K, is less robust to the compounded variability of temporal drift, motion artifacts, and changing physiological conditions in 26K.

In contrast, SAS-Net maintains strong 26K performance, suggesting that its more complex generative architecture—which separately models content and style through dedicated pathways—provides greater capacity for handling diverse domain shifts. Deformation-based methods (VoxelMorph, TransMorph) achieve  $\text{NCC} \leq 0.74$  on 26K, confirming that domain-shift handling remains essential regardless of dataset scale.

### 3.3 Computational Efficiency

table 2 compares the computational cost of GPEReg-Net against baseline methods, benchmarked on an NVIDIA V100 GPU with input size  $512 \times 256$ .

**Table 2.** Computational efficiency comparison. Parameters (M), inference latency (ms), and throughput (FPS) benchmarked on a V100 GPU with  $512 \times 256$  input.

Method	Params (M)	Latency (ms)	FPS
VoxelMorph [2]	0.10	3.06	327
TransMorph [3]	0.17	2.85	351
SAS-Net [12]	3.35	27.21	37
<b>GPEReg-Net (Ours)</b>	3.40	14.52	69

GPEReg-Net achieves 69 FPS with 14.52 ms latency, representing a  $1.87 \times$  speedup over SAS-Net (37 FPS, 27.21 ms) despite having comparable parameter counts (3.40M vs. 3.35M). The efficiency gain comes from the simpler decoding architecture: three AdaIN blocks with direct feature modulation are computationally lighter than SAS-Net’s multi-pathway generative decoder. While the lightweight deformation-based methods (VoxelMorph at 327 FPS, TransMorph at 351 FPS) are substantially faster due to their small parameter counts, their registration quality is far below the scene-appearance methods, making them impractical for the OR-PAM application. GPEReg-Net’s 69 FPS throughput is sufficient for real-time OR-PAM processing pipelines.

### 3.4 Temporal Consistency Evaluation

Beyond single-frame alignment quality, we evaluate temporal consistency across consecutive frames on the 26K dataset using the temporal metrics defined in section 3.1. table 3 reports the results on 2,691 consecutive frame pairs, with

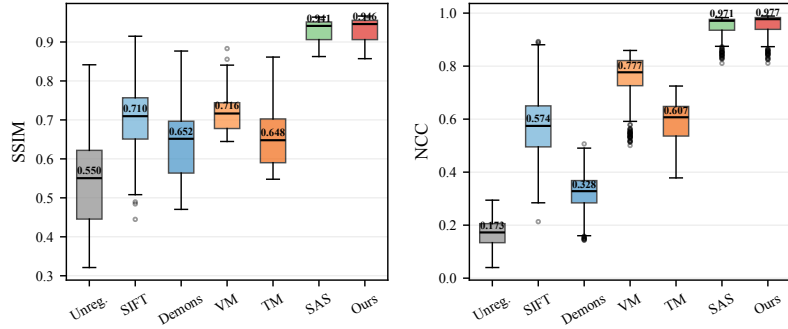


**Fig. 4.** Distribution of registration metrics on OR-PAM-Reg-4K (432 test samples). Box plots show the median, interquartile range, and outliers for NCC, SSIM, and PSNR across all methods. GPEReg-Net exhibits tight distributions with high medians, confirming consistent registration quality across diverse test samples.

reference ceiling values  $TNCC_{ref} = 0.963$  and  $TSSIM_{ref} = 0.923$  computed from odd-only columns.

**Table 3.** Temporal consistency evaluation on OR-PAM-Reg-Temporal-26K (2,691 consecutive frame pairs). TNCC and TSSIM measure inter-frame coherence of consecutive merged frames; TNCG and TSSG measure deviation from reference ceilings. Best in **bold**, second best underlined.

Method	NCC $\uparrow$	SSIM $\uparrow$	TNCC $\uparrow$	TSSIM $\uparrow$	TPSNR $\uparrow$	TNCG $\downarrow$	TSSG $\downarrow$
Odd-only ref	—	—	0.963	0.923	32.07	—	—
<i>Traditional Methods</i>							
SIFT [9]	0.752	0.745	0.891	0.855	28.14	0.0726	0.0683
Demons [21]	0.347	0.634	0.938	0.897	30.20	0.0259	0.0261
Optical Flow [7]	0.089	0.516	0.923	0.889	29.62	0.0404	0.0348
SyN [1]	0.505	0.691	0.923	0.890	29.92	0.0401	0.0336
<i>Deep Learning Methods</i>							
VoxelMorph [2]	0.741	0.594	0.893	0.754	27.02	0.0702	0.1700
TransMorph [3]	0.693	0.653	0.910	0.798	27.54	0.0538	0.1250
SAS-Net [12]	<b>0.994</b>	<b>0.972</b>	<u>0.967</u>	<u>0.937</u>	<u>32.59</u>	<b>0.0038</b>	<b>0.0134</b>
<b>GPEReg-Net (Ours)</b>	<u>0.921</u>	0.634	<b>0.969</b>	<b>0.944</b>	<b>33.03</b>	<u>0.0056</u>	<u>0.0202</u>

Despite lower intra-frame quality on 26K ( $NCC = 0.921$ ), GPEReg-Net achieves the highest absolute temporal coherence with  $TNCC = 0.969$  and  $TSSIM = 0.944$ , surpassing SAS-Net ( $TNCC = 0.967$ ). The GPE module provides natural temporal regularization: cross-frame attention produces temporally coherent scene representations that improve inter-frame consistency beyond the reference ceiling ( $TNCC_{ref} = 0.963$ ). While GPEReg-Net’s temporal gaps ( $TNCG = 0.006$ ,  $TSSG = 0.020$ ) exceed SAS-Net’s (0.004, 0.013), this reflects stronger temporal enhancement—both methods exceed the reference ceiling, with GPEReg-Net achieving the highest absolute  $TNCC$ .

### 3.5 Analysis of Scene-Appearance Disentanglement

The effectiveness of scene-appearance disentanglement can be understood through the complementary roles of the two encoders. The SceneEncoder, via instance normalization, strips per-instance intensity statistics from feature maps, retaining only spatial structure. The AppearanceEncoder, through global average pooling, discards spatial information and retains only intensity statistics. The AdaIN operation in the decoder then recombines these orthogonal representations: it uses the scene features as the spatial template and the appearance code to set the intensity distribution, effectively translating the moving image into the target domain while preserving its structural content.

This disentanglement is particularly well-suited for bidirectional OR-PAM registration, where the domain shift is *global* (all backward columns share the same systematic intensity difference from forward columns) rather than spatially varying. The 32-dimensional appearance code is sufficient to capture this global shift, while the 64-dimensional scene features preserve the fine-grained vascular structure needed for high-fidelity reconstruction. The deterministic nature of the framework avoids the feature uncertainty that affects probabilistic models [15]. The strong 4K results (SSIM = 0.932, PSNR = 34.49 dB) confirm this design, while the 26K degradation suggests that the disentanglement assumption partially breaks down under extended temporal variability where the domain shift becomes more heterogeneous.

## 4 Conclusion

We present GPEReg-Net, a position-aware scene-appearance disentanglement framework for bidirectional OR-PAM registration. By decomposing images into domain-invariant scene features and global appearance codes, and reconstructing registered outputs via AdaIN modulation, the framework avoids explicit deformation field estimation while achieving strong registration quality. On OR-PAM-Reg-4K, GPEReg-Net achieves SSIM of 0.932 and PSNR of 34.49 dB, surpassing SAS-Net by 3.8% and 1.99 dB respectively, while running 1.87 $\times$  faster.

The Global Position Encoding module introduces temporal awareness through learnable embeddings, sinusoidal encoding, and cross-frame attention, enabling the network to leverage neighboring frame context during inference. However, evaluation on OR-PAM-Reg-Temporal-26K reveals limitations: the fixed-capacity learnable embedding table and the global disentanglement assumption degrade under high temporal variability and heterogeneous domain shifts encountered in extended longitudinal acquisitions.

These findings suggest two directions for future work: (1) adaptive position encoding that can generalize to variable-length sequences without fixed embedding tables, and (2) spatially-aware appearance modeling that can capture locally varying domain shifts for improved robustness in longitudinal imaging studies.

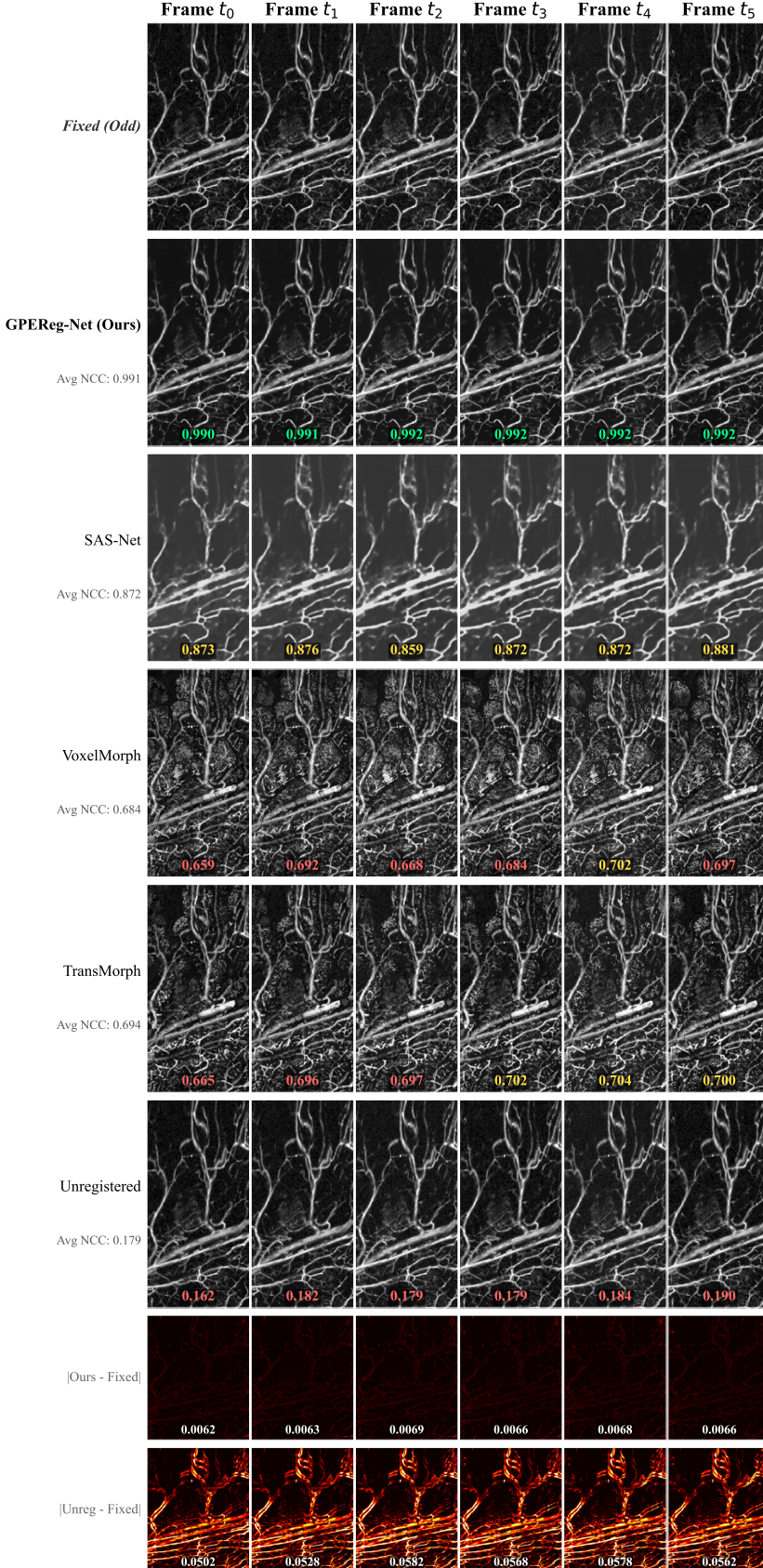


**Fig. 5.** Registration quality visualization on OR-PAM-Reg-Temporal-26K. The first row shows the fixed image (odd columns) as reference. Subsequent rows show registered *even columns only* (the actual model output) for each method across six consecutive frames. The last two rows show the absolute difference between the registered output and the fixed image.

## References

1. Avants, B.B., Epstein, C.L., Grossman, M., Gee, J.C.: Symmetric diffeomorphic image registration with cross-correlation: Evaluating automated labeling of elderly and neurodegenerative brain. *Med. Image Anal.* **12**(1), 26–41 (Feb 2008) [2](#), [8](#), [11](#)
2. Balakrishnan, G., Zhao, A., Sabuncu, M.R., Guttag, J., Dalca, A.V.: VoxelMorph: A learning framework for deformable medical image registration. *IEEE Trans. Med. Imaging* **38**(8), 1788–1800 (Aug 2019) [2](#), [8](#), [10](#), [11](#)
3. Chen, J., Frey, E.C., He, Y., Segars, W.P., Li, Y., Du, Y.: TransMorph: Transformer for unsupervised medical image registration. *Med. Image Anal.* **82**, 102615 (Nov 2022) [2](#), [8](#), [10](#), [11](#)
4. Chen, J., Liu, Y., Wei, S., Bian, Z., Subramanian, S., Carass, A., Prince, J.L., Du, Y.: A survey on deep learning in medical image registration: New technologies, uncertainty, evaluation metrics, and beyond. *Med. Image Anal.* **100**, 103385 (Feb 2025) [2](#)
5. Cho, S., Kim, M., Ahn, J., Kim, Y., Lim, J., Park, J., Kim, H.H., Kim, W.J., Kim, C.: An ultrasensitive and broadband transparent ultrasound transducer for ultrasound and photoacoustic imaging in-vivo. *Nat. Commun.* **15**(1), 1444 (Feb 2024) [1](#)
6. Cikaluk, B.D., Restall, B.S., Haven, N.J.M., Martell, M.T., McAlister, E.A., Zemp, R.J.: Rapid ultraviolet photoacoustic remote sensing microscopy using voice-coil stage scanning. *Opt. Express* **31**(6), 10136–10149 (Mar 2023) [1](#)
7. Horn, B.K., Schunck, B.G.: Determining optical flow. *Artif. Intell.* **17**(1-3), 185–203 (Aug 1981) [2](#), [8](#), [11](#)
8. Huang, X., Belongie, S.: Arbitrary style transfer in real-time with adaptive instance normalization. In: Proc. IEEE Int. Conf. Comput. Vis. (ICCV). pp. 1501–1510 (2017) [2](#), [4](#)
9. Lowe, D.G.: Distinctive image features from scale-invariant keypoints. *Int. J. Comput. Vis.* **60**(2), 91–110 (Nov 2004) [2](#), [8](#), [11](#)
10. Maraghechi, S., Hoefnagels, J.P.M., Peerlings, R.H.J., Geers, M.G.D.: Correction of scan line shift artifacts in scanning electron microscopy: An extended digital image correlation framework. *Ultramicroscopy* **187**, 144–163 (Apr 2018) [1](#)
11. Qin, J.: Progressive contrast registration for high-fidelity bidirectional photoacoustic microscopy alignment. *arXiv preprint arXiv:2602.13304* (2026) [2](#)
12. Qin, J.: SAS-Net: Scene-appearance separation network for robust spatiotemporal registration in bidirectional photoacoustic microscopy (2026), <https://arxiv.org/abs/2602.09050> [2](#), [8](#), [10](#), [11](#)
13. Qin, J., Liu, F., Zong, L.: BC-PMJRS: A brain computing-inspired predefined multimodal joint representation spaces for enhanced cross-modal learning. *Neural Networks* **188**, 107449 (Apr 2025) [2](#)
14. Qin, J., Liu, K., Cai, Y., Ji, T., Liu, F.: MTLP-MDG: Multi-task learning framework using probabilistic distribution perception for missing data generation. In: 2025 International Joint Conference on Neural Networks (IJCNN). pp. 1–8 (2025) [7](#)
15. Qin, J., Peng, B., Liu, F., Cheng, G., Zong, L.: DUAL: Dynamic uncertainty-aware learning. *arXiv preprint arXiv:2506.03158* (2025) [12](#)
16. Qin, J., Wang, Y.: Learning domain-invariant representations for cross-domain image registration via scene-appearance disentanglement. *arXiv preprint arXiv:2601.08875* (2026) [2](#)

17. Qin, J., Xu, Y., Lu, Z., Zhang, X.: Alternative telescopic displacement: An efficient multimodal alignment method. arXiv preprint arXiv:2306.16950 (2023) [2](#)
18. Ronneberger, O., Fischer, P., Brox, T.: U-Net: Convolutional networks for biomedical image segmentation. In: Medical Image Computing and Computer Assisted Intervention – MICCAI 2015. pp. 234–241. Springer (2015) [3](#)
19. Shintate, R., Ishii, T., Ahn, J., Kim, J.Y., Kim, C., Saijo, Y.: High-speed optical resolution photoacoustic microscopy with MEMS scanner using a novel and simple distortion correction method. *Sci. Rep.* **12**(1), 9221 (June 2022) [1](#)
20. Vaswani, A., Shazeer, N., Parmar, N., Uszkoreit, J., Jones, L., Gomez, A.N., Kaiser, L., Polosukhin, I.: Attention is all you need. In: Advances in Neural Information Processing Systems (NeurIPS). pp. 5998–6008 (2017) [2](#), [5](#)
21. Vercauteren, T., Pennec, X., Perchant, A., Ayache, N.: Diffeomorphic demons: Efficient non-parametric image registration. *NeuroImage* **45**(1), S61–S72 (Mar 2009) [2](#), [8](#), [11](#)
22. Wang, L.V., Hu, S.: Photoacoustic tomography: In vivo imaging from organelles to organs. *Science* **335**(6075), 1458–1462 (Mar 2012) [1](#)
23. Wang, Z., Bovik, A.C., Sheikh, H.R., Simoncelli, E.P.: Image quality assessment: From error visibility to structural similarity. *IEEE Trans. Image Process.* **13**(4), 600–612 (Apr 2004) [7](#)
24. Yang, F., Wang, Z., Shi, W., Wang, M., Ma, R., Zhang, W., Li, X., Wang, E., Xie, W., Zhang, Z., Shen, Q., Zhou, F., Yang, S.: Advancing insights into in vivo meningeal lymphatic vessels with stereoscopic wide-field photoacoustic microscopy. *Light Sci. Appl.* **13**(1), 96 (Apr 2024) [1](#)
25. Yao, J., Wang, L., Yang, J.M., Maslov, K.I., Wong, T.T.W., Li, L., Huang, C.H., Zou, J., Wang, L.V.: High-speed label-free functional photoacoustic microscopy of mouse brain in action. *Nat. Methods* **12**(5), 407–410 (May 2015) [1](#)
26. Yao, J., Wang, L.V.: Photoacoustic microscopy. *Laser Photon. Rev.* **7**(5), 758–778 (2013) [1](#)
27. Zhang, H.F., Maslov, K., Stoica, G., Wang, L.V.: Functional photoacoustic microscopy for high-resolution and noninvasive in vivo imaging. *Nat. Biotechnol.* **24**(7), 848–851 (July 2006) [1](#)
28. Zhang, T., Yan, C., Lan, X.: OR-PAM-Reg-4K: A benchmark dataset for bidirectional OR-PAM registration (2026) [7](#)
29. Zhang, T., Yan, C., Lan, X.: OR-PAM-Reg-Temporal-26K: A large-scale longitudinal benchmark for bidirectional OR-PAM registration (2026) [7](#)